Astronomy & Astrophysics

Comparison of the star formation in X-ray-selected AGN in eFEDS with that of star-forming galaxies

G. Mountrichas[1], V. Buat[2,3], G. Yang[4,5], M. Boquien[6], D. Burgarella[2], L. Ciesla[2], K. Malek[7,2], and R. Shirley[8,9]

[1] Instituto de Fisica de Cantabria (CSIC-Universidad de Cantabria), Avenida de los Castros, 39005 Santander, Spain
e-mail: gmountrichas@gmail.com
[2] Aix Marseille Univ, CNRS, CNES, LAM Marseille, France
[3] Institut Universitaire de France (IUF), Paris, France
[4] Department of Physics and Astronomy, Texas A&M University, College Station, TX 77843-4242, USA
[5] George P. and Cynthia Woods Mitchell Institute for Fundamental Physics and Astronomy, Texas A&M University, College Station, TX 77843-4242, USA
[6] Centro de Astronomía (CITEVA), Universidad de Antofagasta, Avenida Angamos 601, Antofagasta, Chile
[7] National Centre for Nuclear Research, ul. Pasteura 7, 02-093 Warszawa, Poland
[8] Astronomy Centre, Department of Physics & Astronomy, University of Southampton, Southampton SO17 1BJ, UK
[9] Institute of Astronomy, University of Cambridge, Madingley Road, Cambridge CB3 0HA, UK

ABSTRACT

We use approximately 1800 X-ray active galactic nuclei (AGN) in the eROSITA Final Equatorial-Depth Survey (eFEDS) that span over two orders of magnitude in X-ray luminosity, $L_{X,2-10\,\mathrm{keV}} \approx 10^{43-45}\,\mathrm{erg\,s^{-1}}$, and compare their star-formation rate (SFR) to that of non-AGN star-forming systems, at $0.5 < z < 1.5$. To this end, we compiled a reference galaxy catalogue of about 17 000 sources. Both samples have the same photometric coverage, from optical to far-infrared. We construct the spectral energy distributions (SEDs) of all sources and fit them using the CIGALE code, using the same templates and parametric grid for both samples, and accounting for the mass incompleteness and exclude quiescent systems from both datasets. This allows us to compare the SFR of the two populations in a uniform manner, minimising systematic effects. Based on our analysis, AGN at low and moderate L_X ($L_{X,2-10\,\mathrm{keV}} < 10^{44}\,\mathrm{erg\,s^{-1}}$) have SFR that is lower than, or at most equal to, that of star-forming galaxies, in agreement with previous studies. The large number of luminous X-ray AGN available in the eFEDS dataset enable us to expand our investigations at higher L_X to test previous, tentative results. At $L_{X,2-10\,\mathrm{keV}} > 10^{44.2}\,\mathrm{erg\,s^{-1}}$, the SFR of AGN appears enhanced by ∼30% compared to that of star-forming sources, for systems with stellar mass in the range of $10.5 < \log[M_*(M_\odot)] < 11.5$, confirming indications found in previous studies. The most massive sources, $\log[M_*(M_\odot)] > 11.5$, present a flat SFR$_\mathrm{norm}$–$L_X$ relation up to $L_{X,2-10\,\mathrm{keV}} \sim 10^{44.5}\,\mathrm{erg\,s^{-1}}$, with SFR similar to that of star-forming galaxies. However, at higher L_X ($L_{X,2-10\,\mathrm{keV}} \sim 10^{45}\,\mathrm{erg\,s^{-1}}$), we find indications that the SFR of these massive AGN hosts may be enhanced compared to that of non-AGN systems.

Key words. galaxies: active – galaxies: fundamental parameters – galaxies: star formation – X-rays: galaxies – galaxies: evolution

1. Introduction

It has been more than two decades since a relation was found between the large-scale properties of galaxies and the mass of the supermassive black holes (SMBH) that live in their centres (e.g., Magorrian et al. 1998; Ferrarese & Merritt 2000; Gebhardt 2000; Kormendy & Ho 2013). Nevertheless, how SMBHs and galaxies interact with each other, despite their difference in physical scale, remains unclear (e.g., Alexander & Hickox 2012).

To shed light on this question, it is important to uncover the mechanisms that drive cold gas onto the SMBH, causing its growth and the eventual birth of an active galactic nucleus (AGN). Several fuelling processes have been proposed in the literature (for a review, see Alexander & Hickox 2012), which vary depending on the redshift, the AGN power (X-ray luminosity, L_X), and the stellar mass, M_*, of the galaxy. Major mergers provide a possible triggering mechanism in the case of luminous AGN (e.g., Bower et al. 2006; Hopkins et al. 2008), while alternative processes have been suggested for lower luminosity AGN, such as minor mergers and disk instabilities (e.g., Genzel 2008; Ciotti et al. 2010). In these cases, large amounts of gas are driven to the centre of galaxies, fuelling the SMBH and setting off the star formation (SF) of the host galaxy. The same mechanism is responsible for triggering both the growth of a SMBH and the growth of the galaxy itself. However, alternative processes have been proposed that activate the SMBH but are decoupled from the SF of the (host) galaxy. For example, in massive systems, diffuse hot gas can be accreted onto the SMBH without first being cooled onto the galactic plane (e.g., Fanidakis et al. 2013).

AGN feedback can also regulate the SF activity, either by heating the gas reservoir of the host galaxy (negative feedback; e.g., Di Matteo et al. 2005; Croton et al. 2006) or by triggering the SF via for example AGN outflows during the gas-rich phase of galaxies (positive feedback; e.g., Zubovas et al. 2013). Understanding the physical mechanisms that trigger AGN activity and the interplay between AGN and SF over a wide range of L_X, redshift, and M_* is fundamental to our understanding of galaxy formation and evolution.

To this end, a number of works have studied the SF of galaxies that host AGN as a function of AGN power (e.g., Lutz 2010; Rosario et al. 2012; Rovilos et al. 2012). Hover, more information can be gained by comparing the SFR of AGN host galaxies

with the SFR of non-AGN systems. At low redshifts ($z < 0.5$), studies found that the SFR of AGN is consistent with that of main sequence (MS) star-forming galaxies (e.g., Santini et al. 2012; Shimizu et al. 2015, 2017; Leslie et al. 2016). Nevertheless, caution should be exercised when comparing results from different studies, because different works use galaxy control samples that include sources with different properties. For instance, as mentioned above, the SFR of X-ray AGN is consistent with that of star-forming galaxies, but appears higher compared with a galaxy sample that includes both star-forming and quiescent systems (Santini et al. 2012) or with a simple mass-matching control sample (see Sect. 7.4 in Shimizu et al. 2017).

Luminous AGN are more rare compared to their lower L_X counterparts and therefore larger cosmic volumes need to be probed to sample them. At higher redshifts, the scarcity of galaxies compelled most X-ray studies to use analytical expressions from the literature to measure the SFR of MS star-forming galaxies (e.g., Schreiber et al. 2015) and compare it with the SFR of AGN (e.g., Rosario et al. 2013; Mullaney et al. 2015; Masoura et al. 2018, 2021; Bernhard et al. 2019). The majority of these works used the $\mathrm{SFR_{norm}}$ parameter to quantify this comparison. $\mathrm{SFR_{norm}}$ is defined as the ratio of the SFR of AGN-dominated systems to the SFR of star-forming galaxies with the same M_* and redshift. Based on the findings of these latter studies, $\mathrm{SFR_{norm}}$ is independent of redshift (Mullaney et al. 2015). Moreover, there is a strong dependence of $\mathrm{SFR_{norm}}$ on X-ray luminosity (Masoura et al. 2021), with more luminous AGN having a narrower $\mathrm{SFR_{norm}}$ distribution that is shifted to higher values and close to those of MS galaxies compared to their lower L_X counterparts (Bernhard et al. 2019).

Recently, a number of studies compiled large non-AGN galaxy samples and compared their SFR with that of X-ray AGN. Florez et al. (2020) used AGN with $L_{X,2-10\,\mathrm{keV}} > 10^{44}\,\mathrm{erg\,s^{-1}}$ in the Boötes field and compared their SFR with a large comparison sample of about 320 000 sources without X-ray AGN. Based on the analysis of these authors, the average SFR of galaxies that host luminous AGN is higher by a factor of ~3−10 compared to sources without AGN, at fixed M_* and redshift.

Mountrichas et al. (2021c) using luminous X-ray AGN in the Boötes field ($L_{X,2-10\,\mathrm{keV}} \sim 10^{43.5-45}\,\mathrm{erg\,s^{-1}}$), demonstrated the importance of using a galaxy control sample to compare the SFR of X-ray with non-AGN systems. Their analysis showed that using an analytical expression from the literature to calculate the SFR of star-forming MS systems can introduce systematic errors that affect the comparison of the SFR of the two populations. Their results indicate that at high L_X ($L_{X,2-10\,\mathrm{keV}} > 2-3 \times 10^{44}\,\mathrm{erg\,s^{-1}}$), AGN hosted by galaxies with stellar mass in the range of $10.5 < \log[M_*(M_\odot)] < 11.5$ have SFR that is enhanced by ~50% compared to their galaxy reference sample. Mountrichas et al. (2022) used X-ray sources from the COSMOS-Legacy survey and applied the same methodology as Mountrichas et al. (2021c). Their AGN spanned lower luminosities ($L_{X,2-10\,\mathrm{keV}} \sim 10^{42.5-44}\,\mathrm{erg\,s^{-1}}$) compared to their X-ray counterparts in Boötes. Based on their results, low- to moderate-luminosity AGN have SFR that is lower than, or at most equal to, that of MS galaxies.

In the present work, we use X-ray AGN from the eROSITA Final Equatorial Depth Survey (eFEDS) field and compare their SFR with those of a galaxy reference catalogue within the same spatial volume. The datasets are described in detail in Sect. 2. We follow the same methodology applied in the previous works of Mountrichas et al. (2021c, 2022) which allows us to compare and complement the results, covering a luminosity baseline of more than 2.5 orders of magnitude ($L_{X,2-10\,\mathrm{keV}} \sim$

$10^{42.5-45}\,\mathrm{erg\,s^{-1}}$) in total. Specifically, we construct the spectral energy distributions (SEDs) of all galaxies and fit them using the CIGALE code (Boquien et al. 2019; Yang et al. 2020, 2022). The models, parametric grid, and quality criteria are described in Sect. 3 and are identical to those used in Mountrichas et al. (2021c, 2022) so as to avoid systematic effects introduced by different templates and parameter space. Our main goal is to use the large number of luminous AGN available in the eFEDS field and examine whether or not the tentative results presented by Mountrichas et al. (2021c) can be confirmed. Our measurements are presented in Sect. 4.

Throughout this work, we assume a flat ΛCDM cosmology with $H_0 = 70.4\,\mathrm{km\,s^{-1}\,Mpc^{-1}}$ and $\Omega_M = 0.272$ (Komatsu et al. 2011).

2. Data

2.1. X-ray sample

In our analysis, we use the X-ray sources observed in the eFEDS field. The catalogue is presented in Brunner et al. (2022). eROSITA (extended ROentgen Survey with an Imaging Telescope Array; Predehl et al. 2021) is the primary instrument on the Spektrum-Roentgen-Gamma (SRG) orbital observatory (Sunyaev et al. 2021). SRG was built to provide a sensitive, wide-field-of-view X-ray telescope with improved capabilities compared to those of *XMM-Newton* and *Chandra*, the two most sensitive targeting X-ray telescopes in operation. The catalogue includes 27 910 X-ray sources[1] detected in the 0.2−2.3 keV energy band with detection likelihoods ≥ 6, which corresponds to a flux limit of $\approx 7 \times 10^{-15}\,\mathrm{erg\,cm^{-2}\,s^{-1}}$ in the 0.5−2.0 keV energy range (Brunner et al. 2022). About 3% of the sources are located at the borders of the field, which implies shorter exposure times, stronger vignetting, and higher background. These sources are excluded from our analysis ("INAREA90" flag). Salvato et al. (2022) presented the multiwavelength counterparts and redshifts of the X-ray sources by identifying their optical counterparts. The DESI Legacy Imaging Survey DR8 (LS8; Dey et al. 2019) was used for counterpart identification because of its homogeneous coverage of the field and its depth. The catalogue also includes *Gaia* (Gaia Collaboration 2021) and WISE (Lang 2014) photometry. Two independent methods were used to find the counterparts of the X-ray sources, NWAY (Salvato et al. 2018) and ASTROMATCH (Ruiz et al. 2018). NWAY is based on Bayesian statistics and ASTROMATCH on the maximum likelihood ratio (Sutherland & Saunders 1992). For 88.4% of the eFEDS point-like sources, the two methods point to the same counterpart. Each counterpart is assigned a quality flag, CTP_QUALITY. Counterparts with CTP_QUALITY ≥ 2 are considered reliable, in the sense that either both methods agree on the counterpart and have assigned a counterpart probability above threshold (CTP_QUALITY = 4 for 20 873 sources) or both methods agree on the counterpart but one method has assigned a probability above threshold (CTP_QUALITY = 3 for 1379 sources), or there is more than one possible counterpart (CTP_QUALITY = 2 for 2522 sources). Only sources with CTP_QUALITY ≥ 2 are included in our analysis (i.e. 24 774 of the 27 910 sources). However, we note that sources with CTP_QUALITY = 2 represent only 4% of our final X-ray sample and their exclusion from our analysis would not affect our results and conclusions (for the final selection of X-ray sources, see Sect. 3). Sources were then

---

[1] An updated catalogue was released on December 3, 2021. This updated version is used in our analysis.

classified into Galactic and extragalactic using a combination of methods and various information (for more details, see Sect. 5 in Salvato et al. 2022). Of the 24 774 X-ray sources, 21 952 are characterised as extragalactic. Galactic sources are rejected from our analysis.

eFEDS has been observed by a number of spectroscopic surveys, such as GAMA (Baldry et al. 2018), SDSS (Blanton et al. 2017), and WiggleZ (Drinkwater et al. 2018). Only sources with secure spectroscopic redshift, *specz*, from the parent catalogues were considered in the eFEDS catalogue (Salvato et al. 2022). Reliable *specz* is available for 6640 sources. Photometric redshifts, *photoz*, were computed for the remaining sources using the LePHARE code (Arnouts et al. 1999; Ilbert et al. 2006) and following the procedure outlined in for example Salvato et al. (2009, 2011) and Fotopoulou et al. (2012). These estimates were compared with those using DNNz, a machine-learning algorithm that uses exclusively HSC photometry (Nishizawa et al., in prep.). A redshift flag is assigned to each source, CTP_REDSHIFT_GRADE. Only sources with CTP_REDSHIFT_GRADE $\geq$ 3 (26 047 of 27 910) are considered in this work. This criterion includes sources with either spectroscopic redshift (CTP_REDSHIFT_GRADE = 5) or for which the *photoz* estimates of the two methods agree (CTP_REDSHIFT_GRADE = 4) or agree within a tolerance level (CTP_REDSHIFT_GRADE = 3; for more details, see Sect. 6.3 of Salvato et al. 2022). We note that 80% of the X-ray sources in our final sample (see Sect. 3) have CTP_REDSHIFT_GRADE $\geq$ 4. Furthermore, we restrict our sources to those within the KiDS+VIKING area (Kuijken et al. 2019; Hildebrandt et al. 2020). Near-infrared (NIR) photometry outside of this region is shallow which significantly affects the accuracy and reliability of the *photoz* calculations (Sect. 6.1 in Salvato et al. 2022). Based on the numbers quoted in Table 7 of Salvato et al. (2022), the accuracy of *photoz* within the KiDs area is $\sigma_{\Delta z/(1+z_{spec})} = 0.049$, and the fraction of outliers ($\Delta z/(1 + z_{specz}) > 0.15$) is 13.9%. This area encompasses 10 294 of the 21 952 extragalactic X-ray sources. Applying the CTP_QUALITY $\geq$ 2 and CTP_REDSHIFT_GRADE $\geq$ 3 criteria reduces the available number of X-ray sources to 10 098 AGN for our analysis.

Liu et al. (2022) performed a systematic X-ray spectral fitting analysis on all the X-ray systems, providing fluxes and luminosities – among other X-ray properties – for the eFEDS sources. Based on the results of these authors, only 10% of the sources are X-ray obscured. The power-law slope calculations are described by a Gaussian distribution with mean value and dispersion of 1.94 ± 0.22. In this work, we use their posterior median, intrinsic (absorption-corrected) X-ray fluxes in the $2-10$ keV energy band.

In our analysis, we measure (host) galaxy properties via SED fitting. In order to get reliable results, it is essential to measure these galaxy properties with the highest possible accuracy. Therefore, we require all X-ray AGN to have the following photometric bands available: $u, g, r, i, z, J, H, K, W1, W2, W4$, where $W1, W2, W4$ are the photometric bands of WISE (Wright et al. 2010), at 3.4 μm, 4.6 μm, and 22] μm, respectively, and the others are the optical and NIR photometric bands of KiDS/VIKING. These criteria reduce the X-ray sources to 5921, that is, ~40% of the 10 098 are rejected. This is due to our requirement for $W4$ (35% of the 10098 do not have a $W4$ measurement). However, $W4$ is important for fitting the mid-infrared (mid-IR) continuum, in particular at $z > 1$. Although we do not apply a requirement for availability of the $W3$ band (WISE band at 12 μm), we note that 83% of the X-ray sources in the final sample (see Sect. 3) have a *W3* measurement.

The X-ray catalogue is also cross-matched with the GAMA-09 photometric catalogue produced by the HELP collaboration (Shirley et al. 2019, 2021), which covers ~35% of the eFEDS area. HELP provides data from 23 extragalactic survey fields imaged by the *Herschel* Space Observatory which form the *Herschel* Extragalactic Legacy Project (HELP). The positions of NIR/IRAC sources are then used as prior information to extract sources in the *Herschel* maps. The XID+ tool (Hurley et al. 2017), which was developed for this purpose, uses a Bayesian probabilistic framework and works with prior positions. The cross-match between the two catalogues was performed using 1″radius and the optical coordinates of the counterpart of each X-ray source. About 10% of the X-ray sources have available *Herschel*/SPIRE photometry.

As mentioned earlier, the main goal of this work is to compare the SFR of X-ray AGN with that of non-AGN systems. In particular, we focus on high X-ray luminosities ($L_{X,2-10 keV} > 10^{44}$ erg s^{-1}) and examine whether or not the indications found by Mountrichas et al. (2021c) in the Boötes field are confirmed by using an X-ray sample with more than twice the number of X-ray sources at high luminosities. Lower luminosities have already been examined by Mountrichas et al. (2022) using the COSMOS sample. AGN at low redshifts do not contribute to $L_{X,2-10 keV} > 10^{44}$ erg s^{-1}. Therefore, we exclude sources below $z < 0.5$. Furthermore, in our SED-fitting process, we use the Gaussian Aperture and Photometry (GAAP) data available in the eFEDS X-ray catalogue and the KiDS/VIKING dataset of the galaxy reference sample. GAAP photometry is performed twice, with aperture setting MIN_APER = 0″.7 and 1″.0. A value for each photometric band with the optimal MIN_APER is provided (for the choice of GAAP aperture size, see Kuijken et al. 2015). GAAP is optimised for calculating *photoz* which requires colour measurements. In the case of extended and low-redshift sources, total fluxes may be underestimated (Kuijken et al. 2019). For these reasons, in the following analysis we use sources at $z > 0.5$.

2.2. Galaxy reference catalogue

To compare the SFR of X-ray AGN with non-AGN systems in a consistent manner, we compiled a galaxy (non-AGN) reference catalogue. We require the same photometric coverage and apply the same SED-fitting analysis in both datasets (see following section). We use the fourth data release catalogue of the KiDS/VIKING imaging survey (Kuijken et al. 2019), which has available optical and NIR photometry and *photoz* measurements for about 100 million galaxies over 1006 square degrees. We restrict the sample to those sources within the eFEDS region (~65 deg^2 overlap) and apply the same requirements for photometric coverage of the X-ray sample. We also restrict the sample to sources with $z > 0.5$ (see previous section). These requirements give us 200 000 galaxies. We cross-match these sources with spectroscopic catalogues from SDSS, WiggleZ, and GAMA which results in 7000 sources with available *specz*. For the remaining sources, we use the *photoz* calculations provided in the KiDS/VIKING dataset. This allows us to significantly increase the size of our reference catalogue, in particular at $z > 1$, where a large fraction of the X-ray sources lie. Photometric redshift was estimated using the BPZ code Benitez (2000). Wright et al. (2019) tested BPZ *photoz* – using the KiDS/VIKING photometry – against several deep spectroscopic surveys. Based on the analysis of these authors, the accuracy of *photoz* is found to be $\sigma_{\Delta z/(1+z_{spec})} = 0.072$. The fraction of outliers ($\Delta z/(1 + z_{specz}) > 0.15$) is ≈17.7%. Finally, we cross-match the galaxy reference catalogue with the GAMA-09

Table 1. Models and values for their free parameters used by CIGALE for the SED fitting.

Parameter	Model/values
SFH: delayed model and recent burst	
Age of the main population	1500, 2000, 3000, 4000, 5000 Myr
e-folding time	200, 500, 700, 1000, 2000, 3000, 4000, 5000 Myr
Age of the burst	50 Myr
Burst stellar mass fraction	0.0, 0.005, 0.01, 0.015, 0.02, 0.05, 0.10, 0.15, 0.18, 0.20
Simple stellar population: Bruzual & Charlot (2003)	
Initial mass function	Chabrier (2003)
Metallicity	0.02 (Solar)
Galactic dust extinction	
Dust attenuation law	Charlot & Fall (2000) law
V-band attenuation A_V	0.2, 0.3, 0.4, 0.5, 0.6, 0.7, 0.8, 0.9, 1, 1.5, 2, 2.5, 3, 3.5, 4
Galactic dust emission: Dale et al. (2014)	
α slope in $dM_{dust} \propto U^{-\alpha}dU$	2.0
AGN module: SKIRTOR)	
Torus optical depth at 9.7 microns $\tau_{9.7}$	3.0, 7.0
Torus density radial parameter p ($\rho \propto r^{-p}e^{-q|\cos(\theta)|}$)	1.0
Torus density angular parameter q ($\rho \propto r^{-p}e^{-q|\cos(\theta)|}$)	1.0
Angle between the equatorial plan and edge of the torus	40°
Ratio of the maximum to minimum radius of the torus	20
Viewing angle	30° (type 1), 70° (type 2)
AGN fraction	0.0, 0.1, 0.2, 0.3, 0.4, 0.5, 0.6, 0.7, 0.8, 0.9, 0.99
Extinction law of polar dust	SMC
$E(B-V)$ of polar dust	0.0, 0.2, 0.4
Temperature of polar dust (K)	100
Emissivity of polar dust	1.6
X-ray module	
AGN photon index Γ	1.9
Maximum deviation from the $\alpha_{ox} - L_{2500\,\text{Å}}$ relation	0.2
LMXB photon index	1.56
HMXB photon index	2.0
Total number of models (X-ray/reference galaxy catalogue)	427 680 000/24 552 000

Notes. For the definition of the various parameters see Sect. 3.1.

photometric catalogue of HELP. Approximately 15% of the galaxies have been detected by *Herschel*.

3. Analysis

3.1. CIGALE

To measure the (host) galaxy properties of the sources in our datasets, we apply SED fitting, using the CIGALE algorithm (Boquien et al. 2019; Yang et al. 2020, 2022). CIGALE allows inclusion of the X-ray flux in the fitting process and has the ability to account for the extinction of the UV and optical emission in the poles of AGN (Yang et al. 2020; Mountrichas et al. 2021a,b; Buat et al. 2021).

For consistency with our previous, similar studies in the Boötes (Mountrichas et al. 2021c) and the COSMOS (Mountrichas et al. 2022) fields, we use the same grid used in these works. This minimises any systematic effects that may be introduced due to the different modules and parametric grid used in the SED fitting process. Table 1 presents the templates and the values for the free parameters. In summary, to fit the galaxy component, we used a delayed star formation history (SFH) model with a function form SFR $\propto t \times \exp(-t/\tau)$. A star formation burst is included (Ciesla et al. 2017; Małek et al. 2018; Buat et al. 2019) as a constant ongoing period of star formation

of 50 Myr. Stellar emission is modelled using the single stellar population templates of Bruzual & Charlot (2003) and is attenuated following Charlot & Fall (2000). The emission of the dust heated by stars is modelled based on Dale et al. (2014), without any AGN contribution. The AGN emission is fit using the SKIRTOR models of Stalevski et al. (2012, 2016). SED decomposition is able to uncover AGN that remain undetected by X-rays (e.g., Pouliasis et al. 2020). To identify such objects in the galaxy reference sample, we also include the AGN module when we fit the SEDs of these sources.

3.2. Quality and reliability examination of the fitting results

To exclude sources that are badly fitted from the analysis, we impose a reduced χ^2 threshold of $\chi_r^2 < 5$. This threshold is based on visual inspection of the SEDs and has been used in previous studies (e.g., Masoura et al. 2018; Mountrichas et al. 2021c; Buat et al. 2021). We note that 94% of the X-ray AGN and 90% of the galaxies in the reference catalogue satisfy this criterion. Applying a more strict criterion, for example $\chi_r^2 < 3$, reduces the number of sources (83% of the X-ray AGN and 85% of the galaxies in the reference catalogue satisfy this criterion), but does not affect the results, which are presented in the following section. We also exclude systems for which CIGALE could not constrain the parameters of interest (SFR, M_*). For

that we apply the same criteria used in previous recent studies (e.g., Mountrichas et al. 2021c, 2022; Koutoulidis et al. 2022; Buat et al. 2021). The method uses the two values that CIGALE provides for each estimated galaxy property. One value corresponds to the best model and the other value (bayes) is the likelihood-weighted mean value. A large difference between the two calculations suggests a complex likelihood distribution and important uncertainties. We therefore only include in our analysis sources with $\frac{1}{5} \leq \frac{\mathrm{SFR_{best}}}{\mathrm{SFR_{bayes}}} \leq 5$ and $\frac{1}{5} \leq \frac{M_{*,\mathrm{best}}}{M_{*,\mathrm{bayes}}} \leq 5$, where $\mathrm{SFR_{best}}$ and $M_{*,\mathrm{best}}$ are the best-fit values of SFR and M_*, respectively and $\mathrm{SFR_{bayes}}$ and $M_{*,\mathrm{bayes}}$ are the Bayesian values estimated by CIGALE. Of the sources in the initial X-ray and galaxy reference catalogues, 78% and 88%, respectively, meet these requirements.

In previous studies in the Boötes (Mountrichas et al. 2021c), the XMM-XXL (Mountrichas et al. 2021a), and the COSMOS (Mountrichas et al. 2022) fields, it was demonstrated that CIGALE can provide reliable SFR and M_* measurements for AGN and galaxies with the same photometric coverage as in the present work, at similar redshifts. We repeat these tests for our samples and reach similar conclusions. Furthermore, the aforementioned studies show that a lack of far-IR photometry does not affect the SFR calculation of CIGALE. Using 10% of our X-ray AGN and 15% of the galaxies in the reference sample with *Herschel* detection, we confirm these previous findings.

Finally, throughout our analysis, we take into account the uncertainties on the SFR and M_* calculations provided by CIGALE. Specifically, we calculate the significance (σ = value/uncertainty) of each stellar mass, σ_{M_*}, and SFR, σ_{SFR}, measurement and weight each source based on these values. The total weight, w_t, assigned to each source is given by the equation

$$w_t = \sigma_{M_*} \times \sigma_{\mathrm{SFR}}. \tag{1}$$

3.3. Identification of non-X-ray AGN systems

In the SED-fitting analysis, we also model the AGN emission in the case of sources in the galaxy reference catalogue. We use CIGALE results to identify systems with an AGN component and exclude them from the galaxy sample. Specifically, we exclude sources with $\mathrm{frac_{AGN}} > 0.2$ (without taking into account the uncertainties on the $\mathrm{frac_{AGN}}$ estimates), consistently with our previous studies (Mountrichas et al. 2021c, 2022). $\mathrm{frac_{AGN}}$ is defined as the ratio of the AGN IR emission to the total IR emission of the galaxy. This excludes ∼50% of the sources in the galaxy reference catalogue. The percentage of sources with a significant AGN component rises from ∼50% at $0.5 < z < 1.5$ to ∼80% at $z > 1.5$.

This increase in the fraction of sources with an AGN component as we move to higher redshifts was also found by Mountrichas et al. (2021c, 2022) and in Boötes and COSMOS. However, in these studies, the percentage was ranging from (15−20)% at $0.5 < z < 1.5$ to (50−60)% at $z > 1.5$. The higher percentages we find using the eFEDS dataset can be explained by the different M_* distributions in the three samples (e.g., Georgakakis et al. 2017; Aird et al. 2018). At $0.5 < z < 1.5$, galaxies from the COSMOS and Boötes catalogues have mean $\log[M_*(M_\odot)] = 10.5$ and 10.7, respectively. However, galaxies in the eFEDS field at the same redshift interval are more massive, with mean $\log[M_*(M_\odot)] = 11.1$. At $z > 1.5$, there is also a difference in the mean M_* for all three fields. Specifically, $\log[M_*(M_\odot)] = 10.7$ and 11.1 in COSMOS and Boötes, respectively, while mean $\log[M_*(M_\odot)] = 11.4$. We split the eFEDS sources in stellar mass bins and confirm that the

median value of $\mathrm{frac_{AGN}}$ increases with increasing M_*. Specifically, for $\log[M_*(M_\odot)] = 9−10$, 10−11, and 11−12, the median $\mathrm{frac_{AGN}}$ is 0.05, 0.09, and 0.16, respectively. For the above M_* bins, the fraction of sources with $\mathrm{frac_{AGN}} > 0.2$ is 17%, 22%, and 40%.

We also note that 35%, 15%, and 7% of the excluded sources have $\mathrm{frac_{AGN}} > 0.2$ at 1, 2, and 3σ, respectively, that is $\mathrm{frac_{AGN}} - \mathrm{frac_{AGN,err}} > 0.2$, $\mathrm{frac_{AGN}} - 2 \times \mathrm{frac_{AGN,err}} > 0.2$, and $\mathrm{frac_{AGN}} - 3 \times \mathrm{frac_{AGN,err}} > 0.2$. The corresponding fractions for the reference catalogue in Boötes are 25%, 10%, and 5% and in COSMOS are 30%, 13%, and 7%, respectively. Therefore, the accuracy with which CIGALE calculates the $\mathrm{frac_{AGN}}$ parameter is similar in the three fields.

Finally, we examine if our results are sensitive to the value of the $\mathrm{frac_{AGN}}$ we select. We apply a stricter criterion to identify sources with an AGN component, namely, $\mathrm{frac_{AGN}} > 0.3$ (without taking into account the uncertainties on the $\mathrm{frac_{AGN}}$ estimates). In this case, ∼30% of the sources in the reference catalogue are excluded. The distributions of SFR and M_* of the remaining sources in the reference sample using $\mathrm{frac_{AGN}} > 0.2$ and $\mathrm{frac_{AGN}} > 0.3$ are identical. The median values of SFR and M_* when we use $\mathrm{frac_{AGN}} > 0.2$ and $\mathrm{frac_{AGN}} > 0.3$ are: $\log[\mathrm{SFR}(M_\odot \, \mathrm{yr^{-1}})] = 1.49$, $\log[M_*(M_\odot)] = 11.18$ and $\log[\mathrm{SFR}(M_\odot \, \mathrm{yr^{-1}})] = 1.48$, $\log[M_*(M_\odot)] = 11.17$, respectively. Furthermore, we confirm that the choice of the value for the $\mathrm{frac_{AGN}}$ does not affect the results presented in the following section.

We conclude that an increased number of sources with (significant) AGN emission is found as we move to higher redshifts and more massive systems. This is in accordance with studies that traced the AGN activity using the distribution of the specific black hole accretion rate and found that the probability of a galaxy to host an AGN (AGN duty cycle) is higher at earlier epochs and for more massive galaxies (e.g., Georgakakis et al. 2017; Yang et al. 2017, 2018; Aird et al. 2018). This criterion significantly reduces the number of available sources in the galaxy reference catalogue at $z > 1.5$, and therefore we restrict our analysis to systems that lie at $z < 1.5$.

3.4. Mass completeness

Our goal is to compare the SFR of X-ray AGN with that of non-AGN galaxy systems at different X-ray luminosities and redshifts. We also examine the role of stellar mass. This comparison could be affected by possible biases that may be introduced by the different mass completeness limits at different redshift intervals. To minimise these biases, we calculate the mass completeness at each redshift bin following the method described in Pozzetti et al. (2010). For these calculations, we use the galaxy reference catalogue because of its larger size. The same method has been applied in previous, similar studies (e.g., Florez et al. 2020; Mountrichas et al. 2021c, 2022).

To estimate the mass completeness limits of our data, we first calculate the limiting stellar mass, $M_{*,\mathrm{lim}}$, of each galaxy using the following expression:

$$\log M_{*,\mathrm{lim}} = \log M_* + 0.4(m - m_{\mathrm{lim}}), \tag{2}$$

where M_* is the stellar mass of each source measured by CIGALE, m is the AB magnitude of the source, and m_{lim} is the AB magnitude limit of the survey. This expression estimates the mass the galaxy would have if its apparent magnitude was equal to the limiting magnitude of the survey for a specific photometric band. We then use the $\log M_{*,\mathrm{lim}}$ of the 20% faintest galaxies at each redshift bin. The minimum stellar mass at each
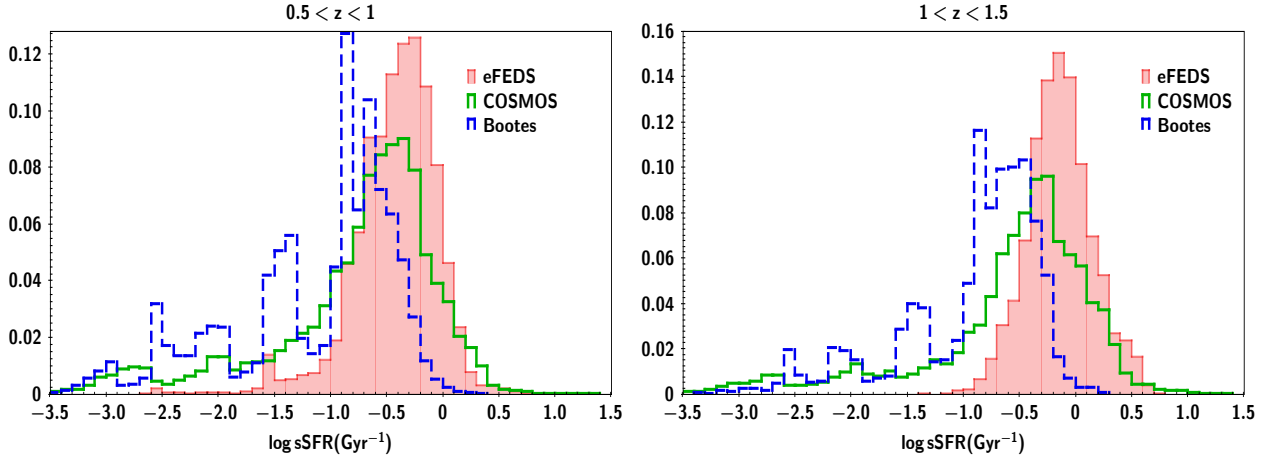
Fig. 1. sSFR distributions in two redshift intervals for the galaxy reference catalogue for sources in the eFEDS field (red shaded histogram). For comparison, we overplotted the distributions from the COSMOS (green line; Mountrichas et al. 2022) and Boötes (blue line; Mountrichas et al. 2021c) fields. Sources in eFEDS do not present the long tails at small sSFR values that are observed for galaxies in COSMOS and Boötes.

Table 2. Number of X-ray AGN and sources in the reference galaxy catalogue after applying the mass completeness limits at each redshift interval.

$\log(M_*/M_\odot)$	Total	$0.5 < z < 1.0$ >9.95	$1.0 < z < 1.5$ >10.67
X-ray catalogue	1867 (1763)	1145 (1092)	722 (671)
Reference galaxy catalogue	17 783 (17 305)	15 261 (14 926)	2522 (2379)

Notes. In the parentheses, we quote the number of sources, when we also exclude quiescent systems.

redshift interval for which our sample is complete is the 95th percentile of $\log M_{*,\mathrm{lim}}$ of the 20% faintest galaxies in each redshift bin.

We use K_s as the limiting band of the samples, in accordance with previous studies (Laigle et al. 2016; Florez et al. 2020; Mountrichas et al. 2021c, 2022) and set $m_{\mathrm{lim}} = 21.2$ (Hildebrandt et al. 2020; Salvato et al. 2022). We find that the stellar mass completeness of our galaxy reference catalogue is $\log[M_{*,95\%\mathrm{lim}}(M_\odot)] = 9.95$ and 10.67 at $0.5 < z < 1.0$ and $1.0 < z < 1.5$, respectively. Using the J or H NIR bands does not significantly change the mass completeness limits. Specifically, we find that $\log[M_{*,95\%\mathrm{lim}}(M_\odot)] = 9.91$ and 9.97 for the J and H bands at $0.5 < z < 1.0$, respectively, and $\log[M_{*,95\%\mathrm{lim}}(M_\odot)] = 10.74$ and 10.57, for J and H at $1.0 < z < 1.5$. We confirm that using any other near-IR band does not affect the overall results or conclusions of our work. This is also true if we use a denser redshift grid ($\Delta z = 0.1$) to calculate the mass completeness of our dataset.

3.5. Exclusion of quiescent systems

In this section, we describe how we identify and reject quiescent systems from our data. Mountrichas et al. (2021c, 2022) used the specific SFR (sSFR (sSFR = $\frac{\mathrm{SFR}}{M_*}$)) of their reference catalogues to define quiescent galaxies. We follow their approach in the following section, which enables us to make a more consistent and fair comparison with their measurements.

In Fig. 1, we plot the distributions of the sSFR of our galaxy catalogue in two redshifts intervals (red shaded histograms). The mean log sSFR values are log sSFR = $-0.47\,\mathrm{Gyr}^{-1}$ and log sSFR = $-0.18\,\mathrm{Gyr}^{-1}$, at $0.5 < z < 1.0$ and $1.0 < z < 1.5$, respectively. This evolution of the mean sSFR with red-

shift is consistent with that from MS studies (see Fig. 11 in Schreiber et al. 2015). Mountrichas et al. (2021c, 2022) identified quiescent systems based on the location of a second lower peak present in the sSFR distributions. Following their approach, we locate these secondary peaks in our distributions. At $0.5 < z < 1.0$, this lower peak is at log sSFR = $-1.5\,\mathrm{Gyr}^{-1}$. At $1.0 < z < 1.5$, the sSFR distribution does not present a second peak. We choose to apply a cut at log sSFR = $-0.6\,\mathrm{Gyr}^{-1}$, which is about 2.5 times lower than the cut at the lower redshift bin, consistently with the shift of mean sSFR values for the two redshift ranges.

Table 2 shows the number of sources remaining after excluding quiescent systems from both the X-ray and the galaxy samples. About ~6% and ~4% of AGN and sources, respectively, in the reference catalogue reside in quiescent systems. These percentages appear low compared to those found by Mountrichas et al. (2022) in the COSMOS field (~25% and 10%, for the AGN and galaxies in the reference sample, respectively), and by Mountrichas et al. (2021c) for sources in Boötes (~30% for both datasets). For comparison, Fig. 1 shows the sSFR distributions of the reference catalogues in COSMOS and Boötes for the same redshift intervals. We notice that in both datasets there is a large tail that expands to lower sSFR values. This tail is less prominent in the case of eFEDS sources for galaxies within $0.5 < z < 1$, and is absent for sources in the highest redshift bin. Sources in the Boötes field present the highest fraction of quiescent systems. This could be due to the high mass completeness limits of the Boötes samples that biased these datasets towards systems with low sSFR values. On the other hand, the brighter luminosities spanned by our X-ray and reference galaxy catalogues compared to the datasets in the COSMOS field may bias our samples against sources with low sSFR
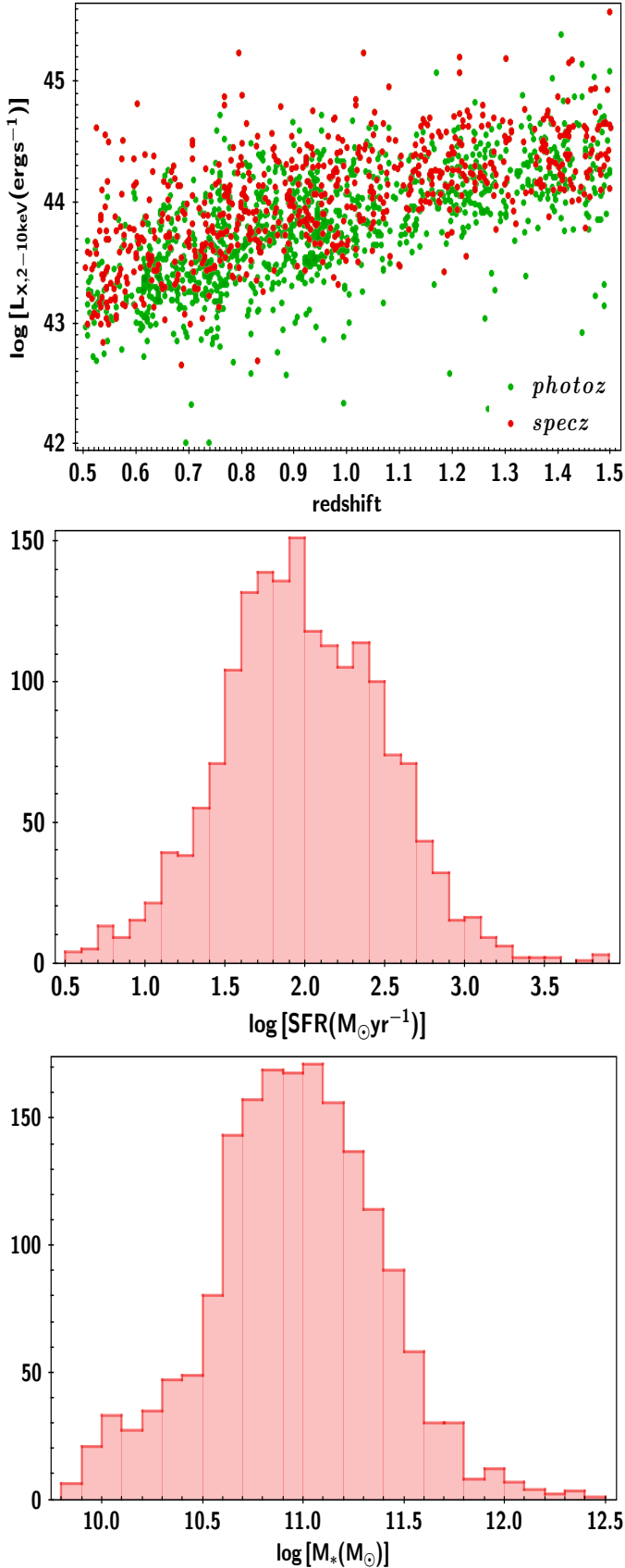
Fig. 2. AGN and galaxy properties of the sources. *Top panel*: X-ray-hard intrinsic luminosity as a function of redshift for the 1763 X-ray AGN in our sample. Of these, 669 (~38%) have *specz*. *Middle panel*: SFR distribution of the 1 763 X-ray AGN. *Bottom panel*: M_* distribution of the X-ray sources.

values (median value of $i = 20.8$ mag in eFEDS, compared to 21.6 and 23.2 for the sources in Boötes and COSMOS).

We explored other possible methods to exclude quiescent systems. Alternatively, we identified as quiescent those sources that have sSFR 1 dex below the mean value at each redshift range (e.g., Salim et al. 2018). Following this approach, we exclude sources with $\log \text{sSFR} < -1.4 \, \text{Gyr}^{-1}$ and $\log \text{sSFR} < -1.15 \, \text{Gyr}^{-1}$, at $0.5 < z < 1.0$ and $1.0 < z < 1.5$, respectively. Regarding the low redshift interval, the sSFR value is almost the same as that used in our analysis above. At the high redshift range, the indicated sSFR value excludes almost none of the quiescent systems.

We then tried a more strict definition for selecting quiescent systems. We excluded those sources that have sSFR values 0.3 dex below the mean value at each redshift range. The results from following these approaches are presented in Appendix A. We find that our results do not change (same trends are observed) regardless of how quiescent systems are defined. Following the stricter definition, SFR$_{\text{norm}}$ values are slightly higher, namely by only 6% on average, and well within the quoted errors of the two measurements. This effect is discussed further in the following section.

Based on these results, in the following analysis, we exclude quiescent systems from our datasets using the location of the low, secondary peaks of the sSFR distributions. The numbers of sources in our final samples are shown in Table 2. The top panel of Fig. 2 presents the position of the X-ray AGN in the L_X–redshift plane. There are 751 (~50% of them with *specz*) X-ray sources with $L_{X,2-10\,\text{keV}} > 10^{44} \, \text{erg s}^{-1}$. This number is about 2.2 times higher than the corresponding number in the Boötes field (Mountrichas et al. 2021c). The middle and bottom panels of Fig. 2 show the SFR and M_* distributions of our X-ray sample, respectively. The median SFR and M_* values are $\log [\text{SFR}(M_\odot \, \text{yr}^{-1})] = 1.97$ and $\log [M_*(M_\odot)] = 11.07$, respectively.

4. Results

4.1. Comparison of the SFR of X-ray AGN with that of star-forming non-AGN systems as a function of L_X

To compare the SFR of X-ray AGN with that of star-forming systems from the reference galaxy catalogue, we use the SFR$_{\text{norm}}$ parameter. SFR$_{\text{norm}}$ is defined as the ratio of the SFR of galaxies that host AGN to the SFR of star-forming galaxies. To calculate this, we use the SFRs that CIGALE has calculated for the 1763 X-ray sources and the 17 305 sources in the reference galaxy. This approach has certain merits. Both samples have the same photometric coverage, the same method (SED fitting) has been applied for the estimation of (host) galaxy properties (SFR, M_*), the same grid has been used for both datasets, and quiescent systems have been excluded following the same criteria for both samples. These similarities minimise a number of systematic effects that may have affected the results of previous studies that used analytical expressions from the literature for the estimation of the SFR of star-forming galaxies (e.g., Mullaney et al. 2015; Masoura et al. 2018; Bernhard et al. 2019).

For the calculation of SFR$_{\text{norm}}$, we follow the method presented in Mountrichas et al. (2021c, 2022). Briefly, the SFR of each X-ray AGN is divided by the SFR of sources in the reference galaxy catalogue that have M_* within ± 0.1 from the M_* of the AGN and lie within $\pm 0.075 \times (1 + z)$ from the AGN. Our measurements are not sensitive to the choice of the box size around the AGN. Changing the above boundaries does not
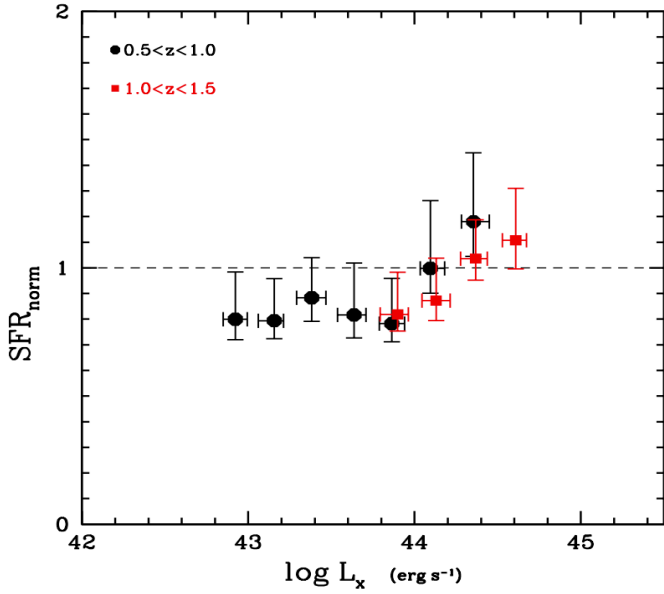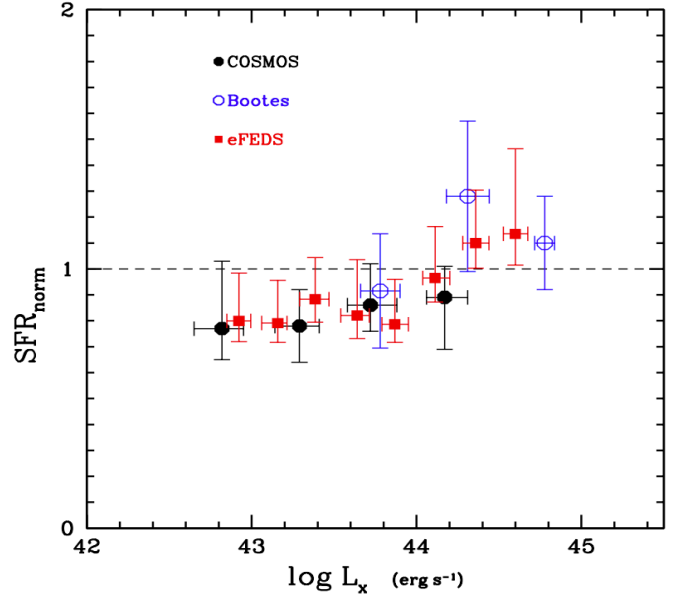
Fig. 3. SFR_{norm} vs. X-ray luminosity. SFR_{norm} and L_X are the median values of our binned measurements, in bins of L_X, with 0.25 dex width. Errors are calculated using bootstrap resampling by performing 1000 resamplings with replacement at each bin. The dashed horizontal line indicates the SFR_{norm} value (=1) for which the SFR of AGN is equal to the SFR of star-forming galaxies. SFR_{norm} values are similar in overlapping L_X regardless of redshift. AGN host-galaxies have SFR that is below or similar to the SFR of MS galaxies at $L_{X,2-10\,keV} < 10^{44}$ erg s^{-1}. At higher X-ray luminosities, SFR_{norm} increases at both redshift intervals.

Fig. 4. SFR_{norm} vs. X-ray luminosity for X-ray AGN in COSMOS, Boötes, and eFEDS. The dashed horizontal line indicates the SFR_{norm} value (=1) for which the SFR of AGN is equal to the SFR of star-forming galaxies. Our measurements in eFEDS (red squares) agree with those from COSMOS, showing that AGN at low to moderate L_X have an SFR that is lower than, or at most equal to, that of galaxies from the reference catalogue. At $L_{X,2-10\,keV} > 10^{44.2}$ erg s^{-1}, our results agree with those from Boötes, revealing a small enhancement (by a factor of $\sim15\%$) of the SFR of AGN compared to sources in the reference catalogue.

change the observed trends, but affects the errors of the calculations (Mountrichas et al. 2021c). The SFR_{norm} is then the median value of these ratios. In this process, each source is weighted based on the uncertainty of its SFR and M_* measurement (see Sect. 3.2). We keep only the X-ray AGN for which the SFR_{norm} has been measured using at least 30 sources from the reference catalogue.

In Fig. 3, we plot the SFR_{norm}–L_X relation for the two redshift intervals we use in our analysis. In overlapping X-ray luminosities, we do not find a dependence of SFR_{norm} on redshift. This is in agreement with previous studies (Mullaney et al. 2015; Mountrichas et al. 2021c, 2022). Based on this result, in Fig. 4, we plot SFR_{norm}–L_X in the total redshift range spanned by our datasets, that is, $0.5 < z < 1.5$. Our goal is to examine the SFR of X-ray AGN relative to the SFR of star-forming galaxies as a function of AGN activity, that is, X-ray luminosity. Figure 4 also shows the results from the Boötes ($0.5 < z < 2.0$; Mountrichas et al. 2021c) and the COSMOS ($0.5 < z < 2.5$; Mountrichas et al. 2022) fields. At low to intermediate X-ray luminosities ($L_{X,2-10\,keV} < 10^{43.5}$ erg s^{-1}), our measurements are in very good agreement with those from COSMOS. Both results show that, in this L_X regime, SFR_{norm} values are systematically below the dashed line, that is, the SFR of AGN is lower compared to that of star-forming galaxies. However, the difference is not statistically significant ($\approx1\sigma$). This implies that galaxies that host X-ray AGN have lower or similar SFR compared to that of star-forming galaxies ($SFR_{norm} \leqslant 1$). At higher L_X, our measurements are in agreement with those in Boötes, showing a small enhancement (on average $\sim15\%$) which is only significant at a level of $\approx1\sigma$.

We perform an additional analysis to check if the SED-fitting parameters influence the obtained results. In Appendix B, we

examine the reliability of CIGALE in constraining the age of the stellar population of X-ray AGN and sources in the reference catalogue. Based on our analysis, the algorithm cannot effectively calculate this parameter. When we fix the stellar age and rerun the SED fitting analysis, we find that, although the observed trends of the SFR_{norm}–L_X relation are not affected, SFR_{norm} values are increased by 17% on average, bringing SFR_{norm} close to one.

The $SFR_{norm} \leqslant 1$ found at $L_{X,2-10\,keV} < 10^{44}$ erg s^{-1} may indicate that the SFR of AGN is lower than that of star-forming galaxies, that is, the AGN reduces the star formation of its host (e.g., Zubovas et al. 2013; Appleby et al. 2020; Lacerda et al. 2020; Shen et al. 2020). However, SFR_{norm} values are statistically consistent with $SFR_{norm} \sim 1$ (within 1σ). Moreover, our analysis shows that the exact amplitude of SFR_{norm} is susceptible to the analysis we follow; for example, it depends on the criteria we apply to exclude quiescent systems (Appendix A) and on the SFH template and parametric grid adopted (Appendix B). We note that in the case of the results from the COSMOS field, the SFR_{norm} values are less affected by the method used to exclude quiescent systems and do not change when we fix the stellar ages. However, these SFR_{norm} measurements are also statistically consistent with one.

We conclude that the SFR of AGN with $L_{X,2-10\,keV} < 10^{44}$ erg s^{-1} is lower than but consistent with that of star-forming galaxies. At higher L_X, we observe an increase in the SFR_{norm} values, which is mild but in agreement with that found in previous studies (Mountrichas et al. 2021c, 2022).

The trends found by our analysis are consistent with those from previous studies. Masoura et al. (2021) found a strong dependence of SFR on L_X using X-ray AGN from the

XMM-XXL dataset. Although our results do not present such a strong evolution of SFR_{norm} with L_X, the overall trends are similar. Specifically, at low to moderate luminosities, the SFRs of AGN tend to be lower than or consistent with those of non-AGN systems, while at higher L_X the SFR of X-ray AGN appears enhanced compared to that of SF galaxies. We also note that Masoura et al. (2021) calculated SFR_{norm} using the analytical expression of Schreiber et al. (2015). As shown in Mountrichas et al. (2021c), this approach may introduce systematic errors that could affect the overall results. Bernhard et al. (2019) found that the SFR_{norm} distribution of AGN with $L_{X,2-10\,keV} < 10^{43.3}\,erg\,s^{-1}$ is lower compared to that of MS galaxies, while more luminous X-ray sources have SFR that is consistent with that of MS SF systems, in agreement with our findings. Santini et al. (2012) used X-ray AGN from the GOODS-S, GOODS-N, and XMM-COSMOS fields and compared their SFR with that of a mass-matched galaxy control sample. Based on their results, the star formation of AGN is consistent with that of SF MS galaxies. Finally, Florez et al. (2020) used X-ray AGN from the Stripe 82 field and compared their SFR with a sample of non-X-ray galaxies. Their analysis showed that X-ray sources have higher SFR than their control galaxy sample by a factor of 3−10. Although our results agree with those of these latter authors regarding the enhancement of the SFR of luminous AGN compared to non-AGN systems, this enhancement is lower based on our measurements.

4.2. $SFR_{norm} - L_X$ for different M_*

Mountrichas et al. (2021c) found indications that the small enhancement of SFR_{norm} with L_X at $L_{X,2-10\,keV} > 10^{44}\,erg\,s^{-1}$ becomes (more) evident when we take into account the M_* of the host galaxy. Following their analysis, we then split our measurements into four M_* bins. Our goal is to use the larger size of the eFEDS sample compared to the Boötes X-ray catalogue and add more datapoints (bins) at the high L_X regime. This allows us to see whether this increase in SFR_{norm} is systematic. Our measurements also include a significantly larger number of X-ray sources in each bin, which will improve the statistical significance of the measurements.

The top left panel of Fig. 5 presents SFR_{norm} versus L_X for galaxies with $10.0 < \log[M_*(M_\odot)] < 10.5$. In agreement with the results in the COSMOS field (Mountrichas et al. 2022), the SFR of galaxies that host AGN is consistent with the SFR of star-forming galaxies (dashed line). There are no results from Boötes in this stellar mass range because of the mass completeness limits of the Boötes sample. The eFEDS and COSMOS datasets do not provide us with enough AGN at $L_{X,2-10\,keV} > 10^{44}\,erg\,s^{-1}$ in this M_* regime to examine whether or not the SFR of X-ray AGN changes compared to star-forming galaxies at higher L_X.

In the top right panel of Fig. 5, we plot SFR_{norm} as a function of L_X for AGN that live in galaxies with stellar mass in the range $10.5 < \log[M_*(M_\odot)] < 11.0$. We also plot the measurements from the COSMOS and Boötes fields. For the latter, the M_* interval is slightly different because of the high mass completeness values of this dataset. At low to intermediate luminosities ($L_{X,2-10\,keV} < 10^{44.}\,erg\,s^{-1}$), our results are in agreement with those from previous studies and in particular with those from the COSMOS dataset, which has larger size compared to the Boötes sample in this luminosity interval. At $L_{X,2-10\,keV} \approx 10^{44.2}\,erg\,s^{-1}$, our measurements confirm the results from the previous studies for increased SFR_{norm}. More importantly, the eFEDS dataset extends this trend at higher X-ray luminosities, that is, up to $L_{X,2-10\,keV} \approx 10^{44.6}\,erg\,s^{-1}$. Based on our results, X-ray AGN that live in galaxies with $10.5 < \log[M_*(M_\odot)] < 11.0$ at $L_{X,2-10\,keV} > 10^{44}\,erg\,s^{-1}$ have enhanced SFR compared to star-forming galaxies by ∼30%, with a statistical significance of ≈2σ.

The bottom left panel of Fig. 5 shows SFR_{norm} as a function of L_X for AGN that live in galaxies with M_*, $11.0 < \log[M_*(M_\odot)] < 11.5$. The trends observed are similar to those we described in the previous stellar mass bin. Specifically, at $L_{X,2-10\,keV} > 10^{44.2}\,erg\,s^{-1}$, the SFR of systems that host AGN is enhanced (by ∼30%) compared to non-AGN sources. We note that the three bins at this L_X interval from the eFEDS sample include 326 X-ray sources compared to 128 from the Boötes catalogue.

We conclude that X-ray AGN that live in galaxies with $10.5 < \log[M_*(M_\odot)] < 11.5$ at $L_{X,2-10\,keV} > 10^{44.2}\,erg\,s^{-1}$ present enhanced SFR (by ∼30%) compared to sources in the reference galaxy catalogue. This increase was also seen in Fig. 4; but when M_* is taken into account, the enhancement is higher and the statistical significance increases.

The bottom right panel of Fig. 5 presents the $SFR_{norm}-L_X$ plane for galaxies with $11.5 < \log[M_*(M_\odot)] < 12.0$. Previous studies found a flat $SFR_{norm}-L_X$ relation for the most massive systems. Although our measurements are in agreement with the previous results, we find an increase of SFR_{norm}, $SFR_{norm} \approx 2.1$ at $L_{X,2-10\,keV} \approx 10^{44.8}\,erg\,s^{-1}$. COSMOS data points do not go up to such high X-ray luminosities. However, X-ray sources in Boötes reach similar L_X, but $SFR_{norm} \sim 1$. The highest L_X bin from the Boötes sample includes 47 X-ray sources compared to 31 sources from eFEDS. Nevertheless, the size of the galaxy reference sample is significantly smaller in Boötes. Specifically, in the Boötes field, in this stellar mass interval, there are 926 galaxies as opposed to 2 753 in eFEDS. As a consequence, for the calculation of the SFR_{norm} of each AGN, in the Boötes sample, each X-ray source has been matched on average with 155 galaxies compared to 495 in the case of AGN in eFEDSs. Restricting the Boötes X-ray sample to those AGN that are matched with >300 galaxies from the reference sample does not change the SFR_{norm} values. The quality of the SED fits of AGN in eFEDS and in Boötes is similar for the sources under investigation, as implied by the median χ^2_{red} values (1.6 in eFEDS vs. 2.0 in Boötes).

About half of the eFEDS AGN (12/31 ≈ 40%) have $\log[SFR(M_\odot\,yr^{-1})] > 3$ compared to 6% (3/47) of the AGN in Boötes. eFEDS sources also expand to $L_{X,2-10\,keV} > 10^{45.0}\,erg\,s^{-1}$ (5/31), but the median L_X of the two bins is similar (median $L_{X,2-10\,keV} = 10^{44.73}\,erg\,s^{-1}$ and $L_{X,2-10\,keV} = 10^{44.62}\,erg\,s^{-1}$, for the eFEDS and Boötes sources, respectively) and we do not see a correlation between SFR and L_X at the narrow L_X range probed by the 78 (31 + 47) AGN. Although previous works did not find a dependence of SFR_{norm} on redshift (e.g., Mullaney et al. 2015; Mountrichas et al. 2021c, 2022), we compare the redshift of the sources included in the two bins of interest. The 31 eFEDS AGN lie at $0.5 < z < 1.5$ (median $z = 1.23$), whereas the 47 X-ray sources from Boötes are within $1.0 < z < 2.0$ (median $z = 1.67$).

Previous studies have not detected a dependence of SFR_{norm} on X-ray obscuration (e.g., Masoura et al. 2021; Mountrichas et al. 2021c). Nevertheless, we examine the X-ray obscuration of the AGN as a possible source of the different results found for this particularly high L_X bin. Of the 47 X-ray sources in Boötes, 32 (68%) are X-ray obscured ($N_H > 21.5\,cm^{-2}$) compared to 10/31 (32%) of the eFEDS AGN. However, we do not find a tendency for lower SFR_{norm} values for the obscured sources in either of the two fields. This is also true if we increase the N_H value used for the X-ray classification ($N_H > 22\,cm^{-2}$). Similar results are found when we
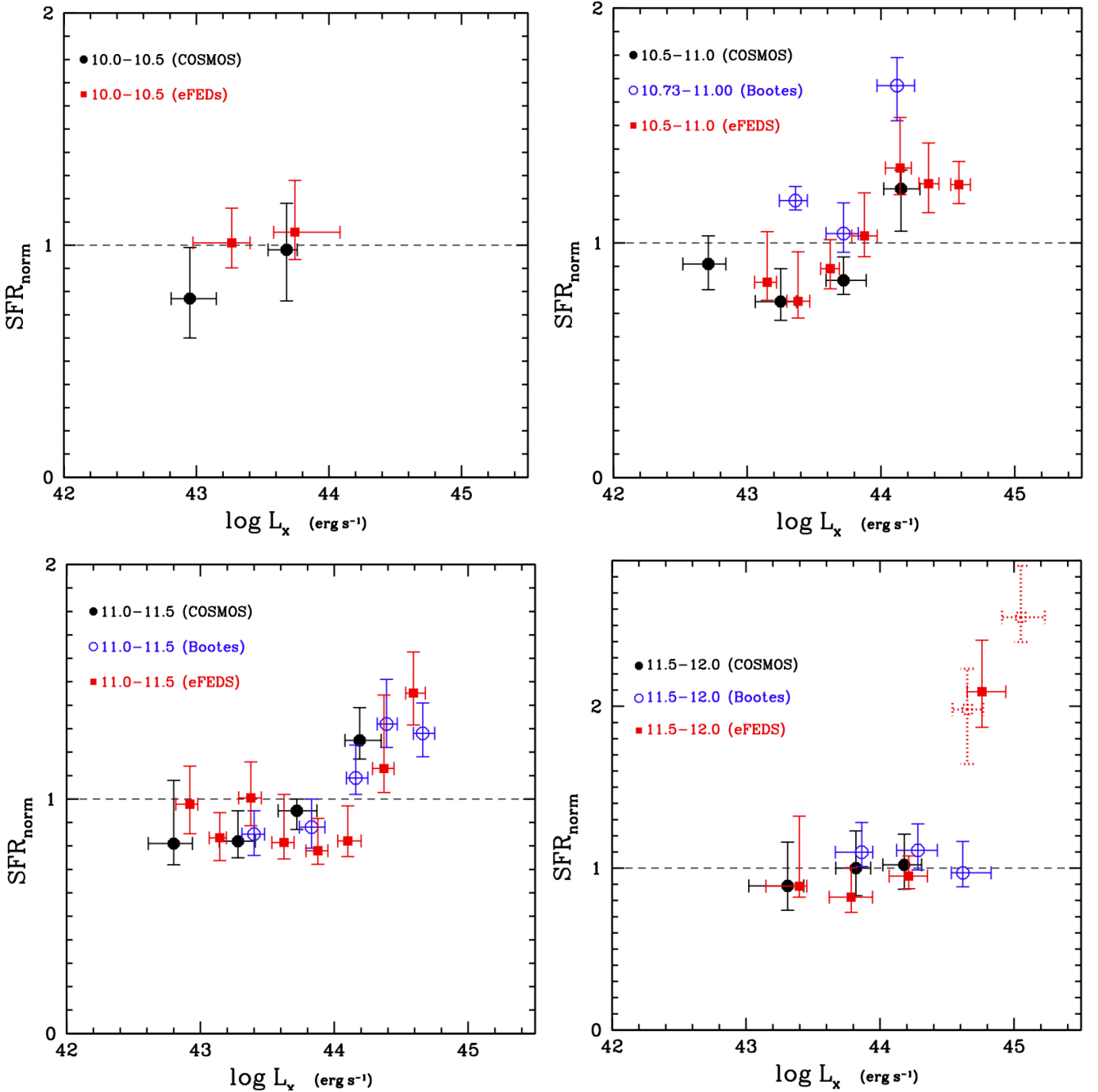
Fig. 5. SFR$_{norm}$ vs. X-ray luminosity for four stellar-mass bins. We complement our results in the eFEDS field (red squares) with those using the COSMOS dataset (Mountrichas et al. 2022) and those from the Boötes sample (Mountrichas et al. 2021c). The dashed horizontal line indicates the SFR$_{norm}$ value (=1) for which the SFR of AGN is equal to the SFR of star-forming galaxies. Errors are calculated using bootstrap resampling. In some cases, the error bars associated to the COSMOS dataset are smaller than those associated to eFEDS. This is due to the finer binning grid used for the eFEDS sample. At low luminosities ($L_{X,2-10 keV} < 10^{44}$ erg s^{-1}), the results from the three studies are in very good agreement. At high luminosities ($L_{X,2-10 keV} > 10^{44}$ erg s^{-1}), our measurements from the eFEDS field confirm the tentative results from the Boötes field, which suggest that AGN host-galaxies with $10.5 < \log[M_*(M_\odot)] < 11.5$ present an approximately 30% higher SFR than star-forming galaxies. In the most massive systems, $\log[M_*(M_\odot)] > 11.5$, our calculations indicate that, in the most luminous systems ($L_{X,2-10 keV} \sim 10^{45}$ erg s^{-1}), the SFR of AGN hosts could be enhanced compared to that of MS galaxies. The two dotted points show the results when we split the highest L_X bin from the eFEDS field into two using an L_X cut at $L_{X,2-10 keV} = 10^{44.8}$ erg s^{-1}.

classify sources based on their inclination angle, i, estimated by CIGALE.

Further investigation of the properties of the sources in the two bins (e.g., AGN fraction, dust attenuation) reveals similar distributions, and median and average values. Their photometric

coverage is also similar. However, eFEDS AGN are more optically luminous compared to their Boötes counterparts (median $i = 19.3$ compared to 21.5).

We also split the highest L_X bin from eFEDS into two using a luminosity cut at $L_{X,2-10 keV} = 10^{44.8}$ erg s^{-1}. WE find that

23 of the 31 AGN have lower L_X than this cut and 8 have higher L_X. The results are shown by the dotted red squares in the bottom right panel of Fig. 5. Although the number of sources included in the two bins is small and no strong conclusions can be drawn, we observe an increase in SFR_{norm} within the L_X range probed by the 31 AGN. However, the lowest L_X bin of the two newly created bins is still significantly higher compared to the highest L_X bin from Boötes; although the L_X ranges spanned by the two bins are very similar.

No strong conclusions can be drawn, but we cannot rule out the possibility that the SFR of the most massive AGN-hosts is enhanced compared to that of MS galaxies at high L_X, in accordance with our findings for less massive systems. It could still be possible that this enhancement occurs at even higher luminosities ($L_{X,2-10\,keV} \sim 10^{45}\,erg\,s^{-1}$). The reason that this trend was not observed in the Boötes field could be a selection effect related to the significantly smaller size (by $\approx 12\times$) of that field compared to eFEDS.

5. Summary and conclusions

We used approximately 1 800 X-ray-selected AGN from the eFEDS field and more than 17 000 galaxies in the same spatial volume ($0.5 < z < 1.5$), and compared the SFR of the two populations. Both samples have the same photometric coverage. We performed SED fitting using the CIGALE algorithm and the same templates and parametric grid for both datasets. We accounted for the mass completeness of the two catalogues and applied a uniform method to exclude quiescent sources from both samples. These allowed us to compare the SFR of X-ray AGN and non-AGN systems in a uniform manner, minimising systematic effects. Furthermore, our analysis and SED fitting grid are identical to those applied in previous studies (Mountrichas et al. 2021c, 2022), which used X-ray sources from different fields (COSMOS, Boötes) and spanned different X-ray luminosities. This allows us to compare and complement our results with theirs and draw a picture regarding the location of X-ray AGN relative to the MS over 2.5 orders of magnitude in L_X ($L_{X,2-10\,keV} \sim 10^{42.5-45}\,erg\,s^{-1}$).

Our results show that, at low to moderate X-ray luminosities, $L_{X,2-10\,keV} < 10^{44}\,erg\,s^{-1}$ X-ray AGN have an SFR that is lower than, or at most equal to, that of star-forming galaxies. This is in agreement with the results of Mountrichas et al. (2022), who studied X-ray sources in the COSMOS field. Mountrichas et al. (2021c) used X-ray data from the Boötes field that span high L_X, and found indications that the SFR of AGN is higher compared to that of MS galaxies at $L_{X,2-10\,keV} > 2-3 \times 10^{44}\,erg\,s^{-1}$. The eFEDS sample is between two and three times larger at these luminosities compared to the Boötes dataset, enabling us to increase the number of datapoints in this L_X regime. Our results confirm these previous tentative results. Specifically, luminous AGN that live in galaxies with $10.5 < \log[M_*(M_\odot)] < 11.5$ have SFR that is higher than that of non-AGN star-forming galaxies by $\sim 30\%$.

Finally, for the most massive systems ($11.5 < \log[M_*(M_\odot)] < 12.0$, we find a flat $SFR_{norm} - L_X$ relation up to $L_{X,2-10\,keV} \sim 10^{44.5}\,erg\,s^{-1}$, with $SFR_{norm} \sim 1$. Although this picture holds at even higher L_X, based on X-ray AGN from the Boötes field (Mountrichas et al. 2021c) in our analysis, we detect significant enhancement of SFR_{norm}, at $L_{X,2-10\,keV} > 10^{44.5}\,erg\,s^{-1}$, that is, higher by a factor of ~ 2. Based on our investigations, we cannot rule out the possibility that in the case of the most massive AGN host galaxies, the SFR is enhanced compared to star-forming galaxies at high L_X, in

agreement with our results for less massive systems, but this enhancement would need to occur at even higher L_X.

Because of their different triggering mechanisms, X-ray AGN constitute a diverse extragalactic population hosted by a variety of galaxies. Our current analysis, complemented by the results from Mountrichas et al. (2021c, 2022) for the Boötes and COSMOS fields, show that it is not only important to compare the SFR of AGN host galaxies with non-AGN systems in a uniform manner, but also to study this in conjunction with a wide range of X-ray luminosities and galaxy properties.
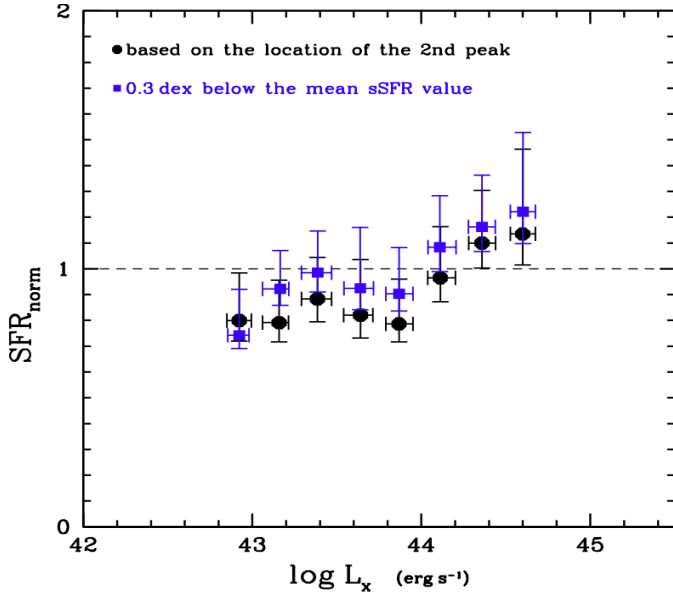
References

Aird, J., Coil, A. L., & Georgakakis, A. 2018, MNRAS, 474, 1225
Alexander, D. M., & Hickox, R. C. 2012, New Astron. Rev., 56, 93
Appleby, S., Davé, R., Kraljic, K., Anglés-Alcázar, D., & Narayanan, D. 2020, MNRAS, 494, 6053
Arnouts, S., Cristiani, S., Moscardini, L., et al. 1999, MNRAS, 310, 540
Baldry, I. K., Liske, J., Brown, M. J. I., et al. 2018, MNRAS, 474, 3875
Benitez, N. 2000, ApJ, 536, 571
Bernhard, E., Grimmett, L. P., Mullaney, J. R., et al. 2019, MNRAS, 483, L52
Blanton, M. R., Bershady, M. A., Abolfathi, B., et al. 2017, AJ, 154, 28
Boquien, M., Burgarella, D., Roehlly, Y., et al. 2019, A&A, 622, A103
Bower, R. G., Benson, A. J., Malbon, R., et al. 2006, MNRAS, 370, 645
Brunner, H., Liu, T., Lamer, G., et al. 2022, A&A, 661, A25
Bruzual, G., & Charlot, S. 2003, MNRAS, 344, 1000
Buat, V., Ciesla, L., Boquien, M., Małek, K., & Burgarella, D. 2019, A&A, 632, A79
Buat, V., Mountrichas, G., Yang, G., et al. 2021, A&A, 654, A93
Chabrier, G. 2003, PASP, 115, 763
Charlot, S., & Fall, S. M. 2000, ApJ, 539, 718
Ciesla, L., Elbaz, D., & Fensch, J. 2017, A&A, 608, A41
Ciotti, L., Ostriker, J. P., & Proga, D. 2010, ApJ, 717, 708
Croton, D. J., Springel, V., White, S. D. M., et al. 2006, MNRAS, 365, 11
Dale, D. A., Helou, G., Magdis, G. E., et al. 2014, ApJ, 784, 83
Dey, A., Schlegel, D. J., Lang, D., et al. 2019, AJ, 157, 168
Di Matteo, T., Springel, V., & Hernquist, L. 2005, Nature, 433, 604
Drinkwater, M. J., Byrne, Z. J., Blake, C., et al. 2018, MNRAS, 474, 4151
Fanidakis, N., Georgakakis, A., Mountrichas, G., et al. 2013, MNRAS, 435, 679
Ferrarese, L., & Merritt, D. 2000, ApJ, 539, 9
Florez, J., Jogee, S., Sherman, S., et al. 2020, MNRAS, 497, 3273
Fotopoulou, S., Salvato, M., Hasinger, G., et al. 2012, ApJS, 198, 1
Gaia Collaboration (Brown, A. G. A., et al.) 2021, A&A, 650, C3
Gebhardt, K., et al. 2000, ApJ, 543, 5
Genzel, R., et al. 2008, ApJ, 687, 59
Georgakakis, A., Aird, J., Schulze, A., et al. 2017, MNRAS, 471, 1976
Hildebrandt, H., Köhlinger, F., van den Busch, J. L., et al. 2020, A&A, 633, A69
Hopkins, P. F., Hernquist, L., Cox, T. J., & Keres, D. 2008, ApJS, 175, 356
Hurley, P. D., Oliver, S., Betancourt, M., et al. 2017, MNRAS, 464, 885
Ilbert, O., Arnouts, S., McCracken, H. J., et al. 2006, A&A, 457, 841
Komatsu, E., Smith, K. M., Dunkley, J., et al. 2011, ApJS, 192, 18
Kormendy, J., & Ho, L. C. 2013, ARA&A, 51, 511
Koutoulidis, L., Mountrichas, G., Georgantopoulos, I., Pouliasis, E., & Plionis, M. 2022, A&A, 658, A35
Kuijken, K., Heymans, C., Hildebrandt, H., et al. 2015, MNRAS, 454, 3500
Kuijken, K., Heymans, C., Dvornik, A., et al. 2019, A&A, 625, A2
Lacerda, E. A. D., Sánchez, S. F., Fernandes, R. C., et al. 2020, MNRAS, 492, 3073
Laigle, C., McCracken, H. J., Ilbert, O., et al. 2016, ApJS, 224, 24
Lang, D. 2014, AJ, 147, 108
Leslie, S. K., Kewley, L. J., Sanders, D. B., & Lee, N. 2016, MNRAS, 455, L82
Liu, T., Buchner, J., Nandra, K., et al. 2022, A&A, 661, A26
Lutz, D., et al. 2010, ApJ, 712, 1287
Magorrian, J., Tremaine, S., Richstone, D., et al. 1998, AJ, 115, 2285
Małek, K., Buat, V., Roehlly, Y., et al. 2018, A&A, 620, A50

Masoura, V. A., Mountrichas, G., Georgantopoulos, I., et al. 2018, A&A, 618, A31

Masoura, V. A., Mountrichas, G., Georgantopoulos, I., & Plionis, M. 2021, A&A, 646, A167

Mountrichas, G., Buat, V., Yang, G., et al. 2021a, A&A, 653, A74

Mountrichas, G., Buat, V., Georgantopoulos, I., et al. 2021b, A&A, 653, A70

Mountrichas, G., Buat, V., Yang, G., et al. 2021c, A&A, 646, A29

Mountrichas, G., Masoura, V., Xilouris, E., et al. 2022, A&A, 661, A108

Mullaney, J. R., Alexander, D. M., Aird, J., et al. 2015, MNRAS, 453, L83

Oesch, P. A., Brammer, G., van Dokkum, P. G., et al. 2016, ApJ, 819, 129

Pouliasis, E., Mountrichas, G., Georgantopoulos, I., et al. 2020, MNRAS, 495, 1853

Pozzetti, L., Bolzonella, M., Zucca, E., et al. 2010, A&A, 523, 23

Predehl, P., Andritschke, R., Arefiev, V., et al. 2021, A&A, 647, A1

Rosario, D. J., Santini, P., Lutz, D., et al. 2012, A&A, 545, A45

Rosario, D. J., Trakhtenbrot, B., Lutz, D., et al. 2013, A&A, 560, A72

Rovilos, E., Comastri, A., Gilli, R., et al. 2012, A&A, 546, A58

Ruiz, A., Corral, A., Mountrichas, G., & Georgantopoulos, I. 2018, A&A, 618, A52

Salim, S., Boquien, M., & Lee, J. C. 2018, ApJ, 859, 11

Salvato, M., Hasinger, G., Ilbert, O., et al. 2009, ApJ, 690, 1250

Salvato, M., Ilbert, O., Hasinger, G., et al. 2011, ApJ, 742, 61

Salvato, M., Buchner, J., Budavári, T., et al. 2018, MNRAS, 473, 4937

Salvato, M., Wolf, J., Dwelly, T., et al. 2022, A&A, 661, A3

Santini, P., Rosario, D. J., Shao, L., et al. 2012, A&A, 540, A109

Schreiber, C., Pannella, M., Elbaz, D., et al. 2015, A&A, 575, A74

Shen, L., Lemaux, B. C., Lubin, L. M., et al. 2020, MNRAS, 494, 5374

Shimizu, T. T., Mushotzky, R. F., Meléndez, M., Koss, M., & Rosario, D. J. 2015, MNRAS, 452, 1841

Shimizu, T. T., Mushotzky, R. F., Meléndez, M., et al. 2017, MNRAS, 466, 3161

Shirley, R., Roehlly, Y., Hurley, P. D., et al. 2019, MNRAS, 490, 634

Shirley, R., Duncan, K., Varillas, M. C. C., et al. 2021, MNRAS, 507, 129

Stalevski, M., Fritz, J., Baes, M., Nakos, T., & Popović, L. Č. 2012, MNRAS, 420, 2756

Stalevski, M., Ricci, C., Ueda, Y., et al. 2016, MNRAS, 458, 2288

Sunyaev, R., Arefiev, V., Babyshkin, V., et al. 2021, A&A, 656, A132

Sutherland, W., & Saunders, W. 1992, MNRAS, 259, 413

Wright, E. L., Eisenhardt, P. R. M., Mainzer, A. K., et al. 2010, AJ, 140, 1868

Wright, A. H., Hildebrandt, H., Kuijken, K., et al. 2019, A&A, 632, A34

Yang, G., Chen, C. T. J., Vito, F., et al. 2017, ApJ, 842, 72

Yang, G., Brandt, W. N., Vito, F., et al. 2018, MNRAS, 475, 1887

Yang, G., Boquien, M., Buat, V., et al. 2020, MNRAS, 491, 740

Yang, G., Boquien, M., Brandt, W. N., et al. 2022, ApJ, 927, 192

Zubovas, K., Nayakshin, S., King, A., & Wilkinson, M. 2013, MNRAS, 433, 3079

Appendix A: Identification of quiescent systems

Fig. A.1. Comparison of the $\text{SFR}_{norm}-\text{L}_X$ for different definitions of quiescent systems. Black circles show the $\text{SFR}_{norm}-\text{L}_X$ measurements when we exclude from the X-ray sample and the galaxy reference catalogue, quiescent sources, based on the location of the lower, second peak in the sSFR distributions. Blue circles present the results when we exclude as quiescent those systems that have sSFR values 0.3 dex below the mean sSFR value. Errors are estimated via bootstrap resampling. The dashed horizontal line indicates the SFR_{norm} value (= 1) for which the SFR of AGN is equal to the SFR of star-forming galaxies.

In this section, we examine whether our measurements are affected by the method we apply to exclude quiescent systems from the X-ray and galaxy reference catalogues. In our analysis, we exclude such sources based on the sSFR distributions. Specifically, we follow the approach of Mountrichas et al. (2021c, 2022) and select quiescent systems based on the location of a second lower peak in the sSFR distributions. However, this peak is not prominent in our sample for sources within $1.0 < z < 1.5$, and the fraction of quiescent galaxies identified is small.

We apply a more strict criterion to exclude quiescent galaxies and examine its effect on our results. Specifically, we reject from our analysis sources that have sSFR that is 0.3 dex below the mean values of the sSFR of galaxies in the reference catalogue. At $0.5 < z < 1.0$, we exclude systems with $\log \text{sSFR} < -0.7\,\text{Gyr}^{-1}$, while at $1.0 < z < 1.5$, we exclude sources with $\log \text{sSFR} < -0.45\,\text{Gyr}^{-1}$. These criteria identify 20% of the X-ray sources and 18% of the sources in the reference catalogue as quiescent systems.

We then measure the SFR_{norn} of each X-ray AGN, as described in Sect. 4, and bin the results in L_X bins with width 0.25 dex for the total redshift range spanned by our datasets. The results are presented in Fig. A.1. Errors have been estimated using bootstrap resampling. For comparison, we also plot the measurements from the samples used in our analysis, i.e. excluding quiescent systems based on the location of the lower, second peak of the sSFR distributions. We notice that the results using the stricter criterion to identify quiescent galaxies are slightly higher (by on average $\sim 6\%$). However, the difference is marginal, that is, the results are consistent within the errors of the two measurements. Most importantly, the observed trends are identical between the two results. In detail, SFR_{norm} is below
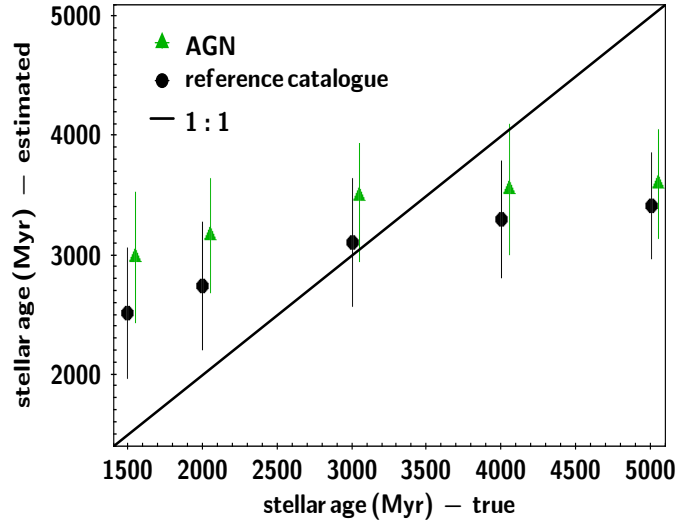
Fig. B.1. Comparison of the age of the main stellar population measurements of galaxies in the reference catalogue and AGN for the estimated and true values from the mock analysis. For both populations, CIGALE overestimates the parameter at $< 3000\,\text{Myr}$. The trend is more evident in the case of X-ray sources. The algorithm underestimates the parameter for older stellar ages. Errors represent the standard deviation of the measurements. AGN measurements have been offset by 50 Myr on the horizontal axis for clarity.

one at $\text{L}_{X,2-10\text{keV}} < 10^{44}\,\text{ergs}^{-1}$ and there is a small increase at higher luminosities, where SFR_{norm} becomes larger than one. This result shows that the (mild) increase in SFR_{norm} we observe at high L_X is not sensitive to how effectively we remove quiescent systems from our samples.

We conclude that the method we choose to identify quiescent systems from our X-ray and galaxy reference catalogues does not affect our overall results and conclusions.

Appendix B: The effect of the adopted SFH on SFR_{norm} calculations

In this section, we examine the effectiveness of CIGALE at constraining the age of the stellar populations of AGN and sources in the reference sample and its effect on the SFR_{norm} measurements. For that purpose, we use the ability of CIGALE to create mock catalogues. These catalogues can be used to assess the validity of a parameter estimation. To create them, the algorithm considers the best fit of each source in the dataset. The code uses the best model flux of each galaxy and inserts a noise extracted from a Gaussian distribution with the same standard deviation as the observed flux. The mock data are then analysed following the same process as for the data (Boquien et al. 2019).

Based on the results presented in Fig. B.1, CIGALE cannot constrain this parameter. Specifically, the algorithm overestimates the ages of the stellar populations both for the X-ray AGN and the sources in the reference catalogue for stellar ages $\leq 3000\,\text{Myr}$ and underestimates them for ages $\geq 4000\,\text{Myr}$. Furthermore, the parameter measurements are systematically lower in the case of non-AGN systems, at least for stellar ages $< 3500\,\text{Myr}$. We also examine whether these results are susceptible to the selection of the SFH module. For this purpose, we run CIGALE again, both for the X-ray and the galaxy reference catalogue, using a delayed SFH template that allows both an instantaneous recent variation of the SFR upwards (burst) and

downwards (quenching; Ciesla et al. 2017; Boquien et al. 2019). The results are not affected by the different SFH module.

We conclude that CIGALE cannot effectively constrain the stellar age of the sources. Now, we examine, if and how this affects the SFR_{norm} calculations. For that purpose, we fix the stellar age of each system to a value that is equal to the age of the universe (in Myr) at the redshift of the source minus 10%-15% and rerun CIGALE, both for the AGN and the reference catalogues. This is based on the expectation that the first galaxies started forming stars a few hundred million years after the big bang (e.g. Oesch et al. 2016).

In Fig. B.2, we plot the SFR_{norm} vs. L_X, for the X-ray AGN within $0.5 < z < 1.5$ for the two runs. We notice that the trends are similar, i.e. SFR_{norm} remains constant at $L_{X,2-10keV} < 10^{44}$ ergs^{-1} and increases at higher L_X. However, SFR_{norm} values are consistently higher, that is by on average $\sim 17\%$, when the stellar age is fixed in the SED-fitting process. However, both measurements are in statistical agreement and therefore our overall conclusion does not change, namely that the SFR of X-ray AGN up to $L_{X,2-10keV} < 10^{44}$ ergs^{-1} is consistent with that of star-forming galaxies, while an increase of SFR_{norm} is observed at higher L_X.
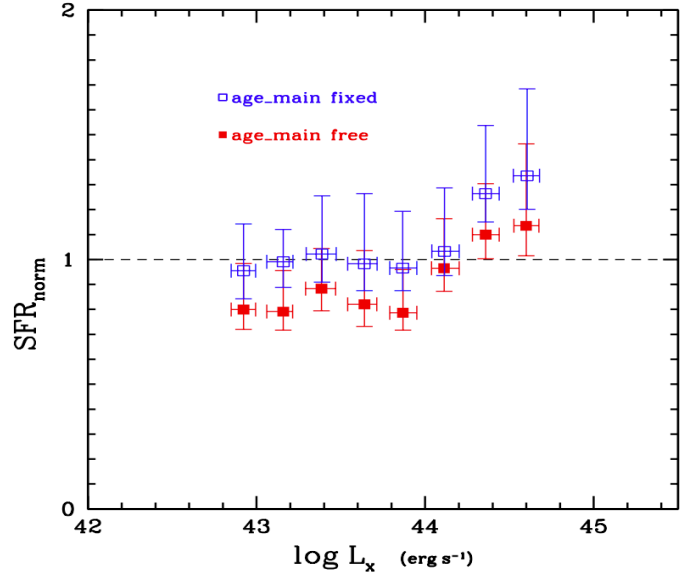
Fig. B.2. Comparison of SFR_{norm} vs. L_X when the stellar age is free and fixed during the SED-fitting process, for the X-ray AGN within $0.5 < z < 1.5$. SFR_{norm} remains constant at $L_{X,2-10keV} < 10^{44}$ ergs^{-1} and increases at higher L_X in both cases. However, SFR_{norm} values are higher by $\sim 17\%$ on average when the stellar age is fixed in the SED-fitting process. Errors are estimated via bootstrap resampling. The dashed horizontal line indicates the SFR_{norm} value (= 1) for which the SFR of AGN is equal to the SFR of star-forming galaxies.